MIT Open Access Articles

An Ultra-Low-Power Pulse Oximeter Implemented With an Energy-Efficient Transimpedance Amplifier

An Ultra-Low-Power Pulse Oximeter Implemented With an Energy-Efficient Transimpedance Amplifier

Maziar Tavakoli, *Student Member, IEEE*, Lorenzo Turicchia, and Rahul Sarpeshkar, *Senior Member, IEEE*

Abstract—Pulse oximeters are ubiquitous in modern medicine to noninvasively measue the percentage of oxygenated hemoglobin in a patient's blood by comparing the transmission characteristics of red and infrared light-emitting diode light through the patient's finger with a photoreceptor. We present an analog single-chip pulse oximeter with 4.8-mW total power dissipation, which is an order of magnitude below our measurements on commercial implementations. The majority of this power reduction is due to the use of a novel logarithmic transimpedance amplifier with inherent contrast sensitivity, distributed amplification, unilateralization, and automatic loop gain control. The transimpedance amplifier, together with a photodiode current source, form a high-performance photoreceptor with characteristics similar to those found in nature, which allows LED power to be reduced. Therefore, our oximeter is well suited for portable medical applications, such as continuous home-care monitoring for elderly or chronic patients, emergency patient transport, remote soldier monitoring, and wireless medical sensing. Furthermore, our design obviates the need for an A-to-D and digital signal processor and leads to a small single-chip solution. We outline how extensions of our work could lead to submilliwatt oximeters.

Index Terms—Biomedical sensor, blood oxygen saturation, low power, medical instrumentation, pulse oximeter, transimpedance amplifier.

I. INTRODUCTION

PULSE oximetry is a fast, noninvasive, easy-to-use, and continuous method for monitoring the oxygen saturation of a patient's blood. Pulse oximeters operate by comparing transmission characteristics of red and infrared light-emitting diode (LED) light through a patient's finger with a photosensor, which provides information on what proportion of the hemoglobin in the blood is dark red and deoxygenated versus bright red and oxygenated. The modulation of the oximeter signal with arterial diameter due to blood pressure variations in between heartbeats helps separate blood transmission characteristics from the unmodulated tissue background.

In modern medical practice, the blood oxygen level is considered one of the important vital signs of the body along with the more traditional ones, such as blood pressure, heart rate, body temperature, and breathing rate. Pulse oximeters provide early information on problems in the respiratory and circulatory systems. They are widely used in intensive care, operating rooms, emergency care, birth and delivery, neonatal and pediatric care, sleep studies, and in veterinary care [1].

The most frequent use of pulse oximeters is in anesthesiology. Tissue oxygenation and, consequently, blood saturation are of extreme importance to anesthesiologists because they administer narcotics to the patient to suppress the central nervous system. This administration stops the patient's desire to breathe and places them in a state where they can no longer meet oxygen demands on their own. In addition, anesthesiologists administer muscle relaxants which stop the ability to breathe and permit airways to collapse. Thus, it is necessary to restore breathing through intubation and artificial respiration. In a sense, the anesthetist becomes the controller for the patient's respiratory system, and the blood oxygen level provides the best feedback variable.

Apart from the aforementioned applications, there is a growing demand today for small, long-lasting, and cheap pulse oximeters suitable for many novel and exciting portable or wearable medical applications [1]. For instance, home-care monitoring for elderly or chronically ill patients is gaining popularity as a continuous and flexible alternative to costly medical supervision in hospitals and nursing homes. Moreover, the military is seeking solutions to remotely monitor the health of soldiers in the battlefield by using light and durable sensor tags attached to their bodies. Other potential applications for such cheap and portable biomedical sensors will also include athlete or farm animal monitoring, emergency patient transport, and wireless sensor networks. Reducing the power consumption of such sensors is a critical step in such applications as power directly dictates battery life, size, and cost which, in turn, influence the dimensions and price of the overall device.

In this paper, we present a pulse-oximeter system which dissipates significantly less power compared to the best low-power commercial pulse oximeters that we could find and measure. LED power, which normally dominates the power requirement of pulse oximeters, can be cut in our device because we employ a novel transimpedance amplifier at the sensor's front end which is more sensitive than other designs to the signal of interest. Moreover, in contrast to traditional A-to-D than DSP approaches, our pulse oximeter performs all of its signal processing in the analog domain and eliminates the need for digital signal processing completely, leading to a very area-efficient single-chip system.

The outline of this paper is as follows: In Section II, we briefly review the basic principles of pulse oximetry. In Section III, we describe the architecture of our low-power pulse oximeter and

M. Tavakoli was with the Department of Electrical Engineering and Computer Science, Massachusetts Institute of Technology, Cambridge, MA 02139 USA. He is now with Linear Technology Corp., North Chelmsford, MA 01863 USA (e-mail: maziar@alum.mit.edu).

L. Turicchia and R. Sarpeshkar are with the Department of Electrical Engineering and Computer Science, Massachusetts Institute of Technology, Cambridge, MA 02139 USA (e-mail: turic@mit.edu; rahuls@mit.edu).

the design and circuit implementation of each of its building blocks. In Section IV, we present experimental results and compare our power consumption with other implementations. In Section V, we conclude by summarizing our contributions.

II. BASIC PRINCIPLES OF PULSE OXIMETRY

The idea behind the operation of pulse oximeters is that hemoglobin changes color from dark red to bright red when oxygenated and reduces its absorption of red light. Hence, if we shine red LED light at 660 nm through one side of a patient's finger and measure the transmitted light on the other side of the patient's finger with a photo sensor (photoreceptor), we can obtain clues regarding the oxygen saturation S_pO_2, the percentage of hemoglobin molecules that are oxygenated in the blood of the patient's finger. However, our absolute measurement will be affected by other tissues, such as skin and bone, that surround the arteries and veins that carry blood. Fortunately, arteries dilate and contract with each heartbeat so that during systole, the phase in which the ventricles of the heart contract and the blood pressure rises, relatively thicker arteries increase the absorption of light, and during diastole, the phase in which the ventricles of the heart relax and blood pressure falls, relatively thinner arteries decrease the absorption of light. By taking the ratio of the light measured by the photoreceptor at the peak and trough of a heartbeat cycle, we can obtain information that is independent of the absolute light intensity of the LED and independent of tissues that do not contain arterial blood (e.g., veins, skin, and bone which do not modulate their absorption with heartbeat cycles). This ratio is still exponentially dependent on the absolute concentration of hemoglobin molecules in the blood (oxygenated or deoxygenated), the absorption coefficient of red light by hemoglobin, and on the thickness variation of the arteries over a heartbeat cycle. To avoid exponential dependency on these unknowns, we can compute the logarithm of the peak-to-trough ratio. If we make another logarithmic peak-to-trough ratio measurement with a 940-nm infrared LED, and take the ratio of our two ratio measurements, any dependence on the absolute concentration of hemoglobin and on the thickness variation of arteries over a heartbeat cycle disappears in our final ratio as these unknowns are the same for both measurements and cancel in the final ratio. Our final ratio gives us information that is dependent only on the absorption coefficients of deoxygenated and oxygenated hemoglobin and on the percentage of hemoglobin that is oxygenated, the desired output of the oximeter S_pO_2. Since the absorption coefficients of deoxygenated and oxygenated hemoglobins are well known from other molecular measurements, we can obtain the percentage of hemoglobin that is oxygenated from a simple calculation.

The intuitive description from before can easily be quantified and is described in detail in [1]. Beer's law describes the attenuation of (monochromatic) light traveling through a medium containing an absorbing substance and predicts it to be an exponential function of the product of three quantities, namely, the distance through the medium, the concentration of the substance, and its intrinsic molecular absorption (extinction) coefficient. It can be shown that the oximeter's desired output is given by

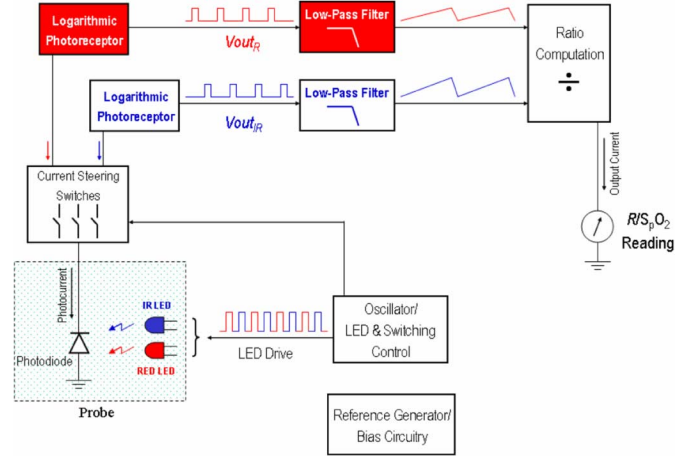$$S_pO_2 = \frac{0.81 - 0.18R}{0.63 + 0.11R} \times 100\% \qquad (1)$$

Fig. 1. Structure of our pulse oximeter system.

where the constants in (1) are related to the absorption (extinction) coefficients of oxygenated and deoxygenated hemoglobin at 660 nm and at 940 nm. In this equation, R represents a parameter called the "ratio of normalized absorbances," the quantity actually measured by pulse oximeters, and is given by

$$R = \frac{\ln(I_{L,R}/I_{H,R})}{\ln(I_{L,IR}/I_{H,IR})} \simeq \frac{i_{ac,R}/I_{DC,R}}{i_{ac,IR}/I_{DC,IR}}. \qquad (2)$$

The symbols I_L, I_H, i_{ac}, and I_{DC} denote the minimum value, maximum value, ac component, and dc component (average) of the red (R) and infrared (IR) light signals that are modulated by the pulsations of arterial blood and detected at the photoreceptor. The ac component of interest in (2) is the signal component at the heart rate (f_p) that is normally around 60–120 beats per minute (bpm) or, equivalently, 1–2 Hz in a healthy adult. The ac/dc terms on the right-hand side of (2) are known to be an excellent approximation to the left-hand side of (2) for the small ac signals and large dc signals that are typically found in pulse oximetry applications since $d(\log(U)) = (dU/U)$ [1]. Typical values of R range from 0.5%–2% [1].

There are some secondary effects, such as the scattering of light in the human tissue or its reflection at the surface of the skin, which are not accounted for in Beer's law. These physical processes, which are very hard to model in a complex medium, such as the human body, necessitate empirical calibration of all pulse oximeters. For example, to calibrate commercial pulse oximeters, a large set of data is obtained in clinical studies from a large number of subjects. The collected data contain information about R provided by the noninvasive pulse oximeter that is paired with actual S_pO_2 readings found by analyzing blood samples of the subjects in a lab. Polynomial equations are then used to find an empirical relationship between R and S_pO_2 that has less error than (1), [1]. After we have discussed how to find R, we shall discuss the calibration of our pulse oximeter.

III. ARCHITECTURE OF OUR LOW-POWER PULSE OXIMETER

A block diagram of our pulse oximeter system is displayed in Fig. 1. The input to the chip is a photocurrent coming from the probe and the output of the chip is another current directly proportional to R. To save power dissipation in the LEDs, the LED drive signals are chopped by a square wave with a small
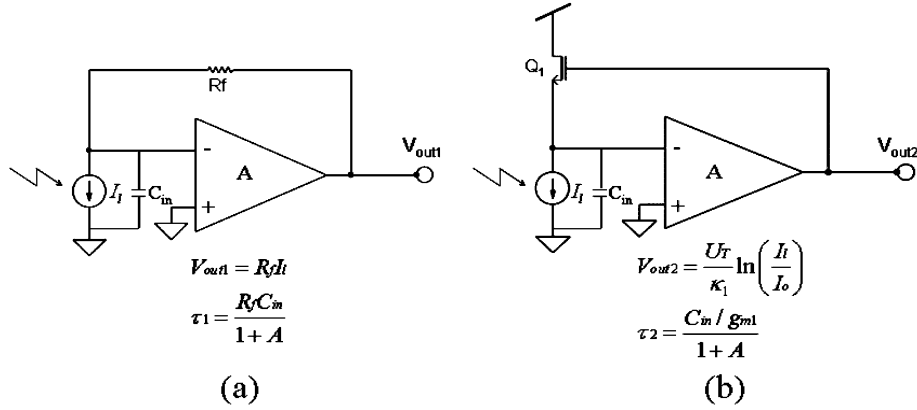
Fig. 2. Schematic of (a) a linear and (b) logarithmic transimpedance amplifier.

duty cycle and a switching frequency f_s (3% and 100 Hz in our setup, respectively). The arterial blood pulsations at the heart rate frequency (f_p) AM modulate the chopped LED light passing through the tissue. Our switching frequency f_s is still much higher than f_p so that aliasing effects are minimal.

The red and IR LEDs are alternatively illuminated and the photocurrent generated by a single photodiode is split, switched, and steered into two different paths (channels), one channel sensitive to the red light, and the other to IR light. The signal-processing unit is composed of our novel transimpedance amplifiers, low-pass filters (LPF), and a ratio computation block. We will now sequentially describe each section of the oximeter system shown in Fig. 1.

A. Novel Transimpedance Amplifiers

The most important building blocks of our pulse oximeter system are its two front-end transimpedance amplifiers (photoreceptors) which convert the light-generated current to voltage. In commercial pulse oximeters, this conversion is often carried out by a classic linear transimpedance amplifier, such as the one shown in Fig. 2(a) and [1]. The amplifier (A) is utilized to attenuate the effect of the typically large parasitic capacitance of the photodiode, thus decreasing the time constant, and increasing the bandwidth of the sensor. However, our pulse oximeter system employs a logarithmic characteristic to convert current to voltage. As displayed in Fig. 2(b), our logarithmic characteristic is achieved by the feedback transistor Q_1 which operates in its subthreshold regime of operation (since I_l is fairly small) and exhibits an exponential I-V characteristic. Other logarithmic transimpedance amplifiers are described in [23].

The key incentive behind the employment of the logarithmic instead of linear sensing is that it is inherently sensitive to the contrast (ac/dc) of the input photocurrent signal since the derivative of a $\log(U)$ function is equal to the derivative of U over U itself: If we Taylor expand the logarithmic large-signal relationship between I_l and V_{out2} shown in the circuit of Fig. 2(b) to find its small-signal output voltage, we obtain

$$v_{\text{ac,out2}} = \left(\frac{dV_{\text{out2}}}{dI_l}\right) i_{\text{ac},l} = \left(\frac{U_T}{\kappa_1} \times \frac{1/I_o}{I_l/I_o}\right) i_{\text{ac},l}$$
$$= \left(\frac{U_T}{\kappa_1}\right) \frac{i_{\text{ac},l}}{I_{\text{DC},l}}. \tag{3}$$

We see that this voltage is indeed proportional to the ac/dc of the input current as expected; κ_1 is the subthreshold exponential coefficient of Q_1, and $U_T = kT/q$ is the thermal voltage [2]. Logarithmic photoreceptors are therefore a perfect fit to oximetry applications. Comparing (2) and (3) reveals that the outputs of the two logarithmic transimpedance amplifiers seen in Fig. 1 are automatically proportional to the numerator $(i_{\text{ac},R}/I_{\text{DC},R})$ and the denominator $(i_{\text{ac},IR}/I_{\text{DC},IR})$ of (2), respectively. Therefore, the exploitation of logarithmic computation saves us the need to explicitly calculate two ac and two dc components and then performs two divisions as in conventional linear systems.

The circuit schematic of a well-known logarithmic transimpedance photoreceptor is shown in Fig. 3, [3]. This photoreceptor was inspired by the operation of biological photoreceptors in turtle cones and bears many of its properties including higher ac gain than dc gain, a contrast-sensitive response, and a relatively wide dynamic range of operation
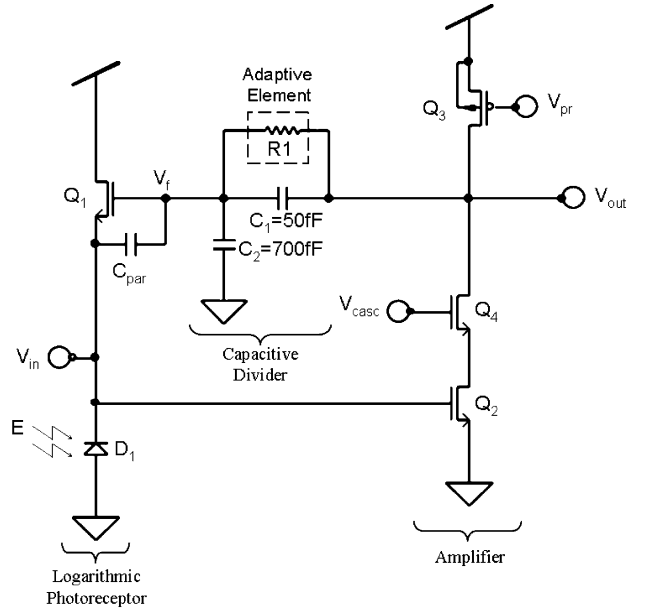

Fig. 3. Circuit schematic of a state-of-the-art logarithmic transimpedance photoreceptor with a single-stage amplifier and adaptive temporal filtering. (All of the transistors in this figure have $W = L = 4.8\ \mu$m.)
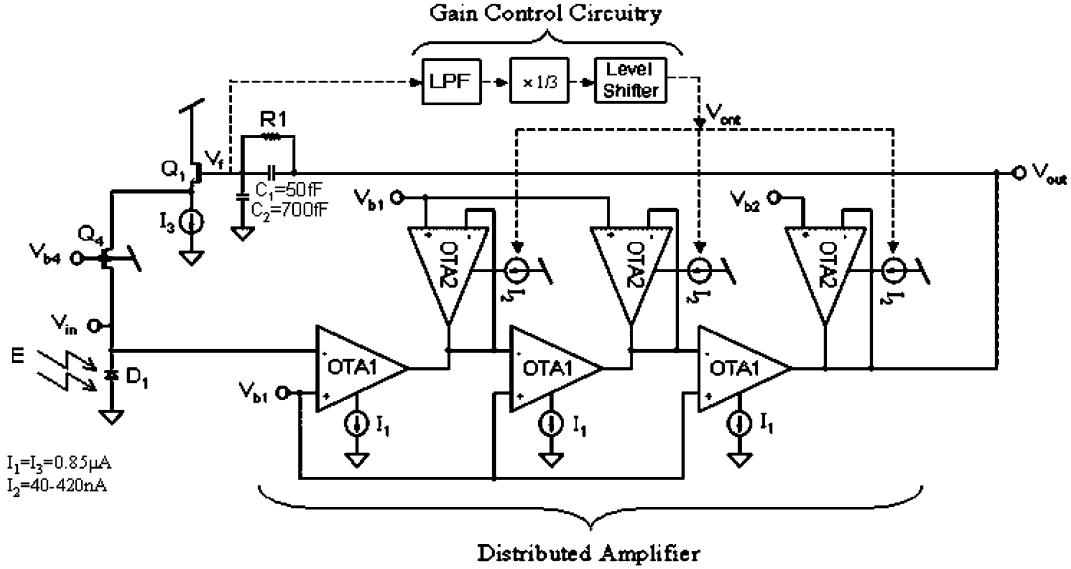
Fig. 4. Circuit schematic of each logarithmic transimpedance amplifier used in our pulse oximeter system of Fig. 1. This circuit employs distributed amplification and automatic loop gain control. (All of the transistors in this figure have $W = L = 4.8 \ \mu m$.)

[4]. The diode D_1 and transistor Q_1 form a logarithmic photoreceptor and transistors Q_2-Q_4 implement a single-stage inverting common-source amplifier, as outlined in Fig. 2(b). The elements C_1, C_2, and R_1 in Fig. 3 form a temporal low-pass (LP) filter in the feedback path, which results in an overall high-pass (HP) characteristic for the photoreceptor and boosts the gain for ac signals (beyond the HP pole frequency). The use of an adaptive $\sin h$ element to realize R_1, a detailed implementation for which may be found in [4], results in a value of around 0.1 Hz for this frequency. The output voltage of the photoreceptor in Fig. 3 for ac signals is equal to

$$v_{ac,out} = \left(\frac{U_T}{\kappa_1} \right) \left(\frac{C_1 + C_2}{C_1} \right) \frac{i_{ac,l}}{I_{DC,l}}. \qquad (4)$$

While this photoreceptor works well for many applications, the limited gain of the simple amplifier and unwanted capacitances in its architecture (i.e., C_{par}) limit the speedup of its light-dependent slow input time constant and restrict its closed-loop bandwidth. Furthermore, the bandwidth of the photoreceptors changes linearly with light intensity, an undesirable property if it is to have a performance invariant with LEDs of varying intensities, in fingers of different thickness, and with different skin pigmentation. Real biological photoreceptors use distributed gain amplification and adaptive feedback to make their bandwidth weakly dependent on intensity [5], [6]. We can take inspiration from their design to further improve the design of this logarithmic transimpedance amplifier (photoreceptor).

Fig. 4 illustrates the circuit schematic of a novel logarithmic transimpedance amplifier that we have employed in the pulse oximetry system of Fig. 1. Our photoreceptor improves on the photoreceptor of Fig. 3 in three ways, which are described in the paragraphs below. Our first improvement is to distribute the gain of the amplifier over three stages, rather than one stage, to increase its gain-bandwidth product (GBW). A high GBW is necessary for attaining large gains in the amplifier and still ensuring that the feedback loop of the photoreceptor is stable. A higher gain for the amplifier results in a larger speedup for the

light-dependent pole at the input of the photoreceptor, thus there is smaller LED light intensity and smaller power dissipation in our pulse oximeter for a given target bandwidth. A high bandwidth is required to ensure that our photoreceptors completely turn ON and settle down in the short ON duration of LED pulses to guarantee proper conversion, distribution, and processing of the input red and IR photocurrents.

The reason for distributing gain is that it is hard to build single-stage amplifiers with a large GBW. A cascade of amplifiers has a significantly larger GBW than a single-stage amplifier with the same gain. In fact, it has been shown in [7] that if the GBW of each amplifying stage is constant, then the time constant for an N-stage amplifier with identical gains per stage is proportional to $N^{1/2}A^{(1/N)}$ versus being proportional to A for the single-stage case (the single stage has the same overall gain A). Intuitively, the higher GBW is attained because, while time constants add in a cascaded-gain system, gains multiply. In other words, a large GBW is achieved in a multistage amplifier because you can build up gain more quickly than you lose bandwidth. Bandwidth considerations help us understand why the gain may have been distributed in many biological systems (e.g., photoreceptors in biology typically have multiple gain stages [6]) and amplification in the cochlea is performed collectively over many stages [8], [9]. RF low-noise amplifiers (LNAs) are usually multistage if a large GBW is required. In many biological systems, a multistage gain topology also allows one to adapt the gain of the topology with a much weaker change in bandwidth [5], [8], [9].

A numerical example helps clarify the dramatic advantages of distributing gain: Suppose that in the transimpedance topology of Fig. 2(b), we want to realize a gain of 8000 in our amplifier to speed up a light pole that initially lies at 1 Hz (open loop) in a typical low light-intensity condition and achieves a closed-loop bandwidth as high as possible. Suppose that first we decide to implement this gain by cascading three gain stages, each having a gain of 20. Assume that each amplifying stage has a GBW of 2×10^6 (in hertz). Therefore, the feedback loop has one open-

loop light pole at 1 Hz, three open-loop amplifier poles at $2 \times 10^6/20 = 100$ kHz, and a loop gain of 8000. Root locus and feedback loop analysis show that when the loop is closed, the light pole moves to 11 kHz. Also, one of the amplifier poles is transferred to 43 kHz while the other two are much higher in frequency. Thus, the closed-loop system acts almost like a first-order system with a bandwidth of about 11 kHz (set by the light pole) and no stability problems. This example also shows that since the light-dependent pole acts as a dominant pole for the system, there are no potential stability problems due to the existence of three amplifier poles.

Now suppose that we want to implement the required 8000 gain with a single amplifying stage. In this case, the feedback loop has one open-loop light pole at 1 Hz, a single open-loop amplifier pole at $2 \times 10^6/8000 = 250$ Hz, and a loop gain of 8000. Note that the amplifier pole is now 400 times slower than the amplifier poles above at the same overall gain, meaning that the effective GBW of the amplifier is much smaller. When the feedback loop is closed, a root locus plot illustrates that these two poles come together and depart from the real axis and form a complex pair at a frequency of 1.4 kHz and with a Q of 5.6. Therefore, not only does the single-stage-amplifier system have a final bandwidth that is almost eight times smaller than the three-stage system, it exhibits poor transient response and large overshoot, which makes it practically unusable. This example demonstrates the merits of distributing the gain over many stages in our transimpedance amplifier design.

As seen in Fig. 4, six operational transconductance amplifier (OTA) blocks form our three-stage amplifier. These blocks have an input–output relationship defined by $i_{out} = G_{mi}(v_{in+} - v_{in-})_{i=1,2}$ where G_{mi} is proportional to I_i. This relationship implies that the OTA2 blocks, in which the output terminal is connected to the negative input terminal, act like resistors of value $1/G_{m2}$. Thus, the total gain of the three-stage amplifier is $(-G_{m1}/G_{m2})^3$. The circuit implementations of the specific OTA1 and OTA2 blocks utilized in our transimpedance amplifiers are displayed in Fig. 5. OTA1 is a cascode differential amplifier with active load. OTA2 is a wide output voltage range differential amplifier [2] that uses the well (body) terminals of the two input PMOS transistors, instead of their gates, to lower the transconductance of the block (i.e., G_{m2}) and increase the overall gain of our distributed amplifier [10].

Our next novel improvement in the transimpedance amplifier of Fig. 4 is to incorporate an adaptive loop gain mechanism to automatically adjust its loop gain based on the light intensity. With an increase in light, V_f, V_{cnt}, I_2, and, finally, G_{m2} rise and the gain of the distributed amplifier drops (and vice versa). The circuit then exhibits less speedup for high light levels (to prevent potential instability due to interactions of light pole and three amplifier poles) and more speedup for low light levels (to achieve the target bandwidth required in our pulse oximetry application).

The voltage V_f is averaged by an LPF so that our gain control mechanism only responds to changes in the average light intensity. Blocks marked "$\times 1/3$" and "Level Shifter" in Fig. 4 adjust the gain and the offset of the control variable V_{cnt}. Since we have three gain stages and the product of the gains of the three stages $(-G_{m1}/G_{m2})^3$ needs to adapt linearly with light intensity, the change in G_{m2} with intensity should follow a $1/3$ power law. The blocks marked "$1/3x$" and "level shifter" implement this power law in the current domain via a $1/3$rd at-
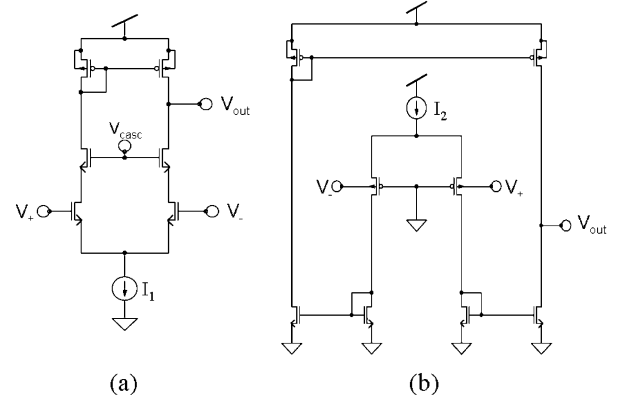

Fig. 5. Circuit implementations of (a) OTA1 blocks and (b) OTA2 blocks utilized in the distributed amplifier of Fig. 4. (All of the transistors in this figure have $W = L = 4.8\ \mu m$.)

tenuation and shift in the log-voltage domain, respectively. The circuits of Fig. 4 implement this condition since V_f changes logarithmically with intensity and the G_{m2} of OTA2 changes exponentially with its gate voltage in subthreshold operation. A more exact analysis shows that this power needs to be $1/(3\kappa)$ if all of the G_{m2} amplifiers operate in subthreshold and $2/(3\kappa)$ if all of the G_{m2} amplifiers operate above threshold. Experimentally, this photoreceptor was able to achieve a closed-loop bandwidth that was nearly invariant over more than three orders of magnitude of light intensity.

In a configuration similar to that of each gain stage of the distributed amplifier, the G_m ratio of two OTAs implements the scaling factor "$\times 1/3$" in the adaptive loop gain circuitry of Fig. 4. However, the transfer curves of these OTAs features a sinh I-V characteristic that is implemented by using a novel sinhR element described in [11]. The sinh resistance quickens the response time of the adaptive loop gain mechanism to large input transients and, thus, improves its stability.

Finally, a common-gate stage (i.e., transistor Q_4) is used in the transimpedance amplifier of Fig. 4 to sense the input photocurrent and convert it to a logarithmic voltage. This transistor removes the unwanted feedthrough coupling due to the gate-to-source capacitance C_{par} in Fig. 3, which limits the speedup and bandwidth of the photoreceptor's transimpedance feedback loop by creating an unwanted zero in it. The gate-to-source capacitance of Q_4 is shorted to an ac ground at V_{b4} in Fig. 4 and does not cause feedthrough. Note that a source-follower stage (i.e., transistor Q_1) is still needed to ensure that no dc current flows through R_1 [4]. However, the feedthrough coupling caused by the gate-to-source capacitance of this source follower is at a very high frequency because I_3 is a relatively large bias current rather than a small light-dependent current so that there are no bandwidth-limiting effects in the loop. The use of Q_4 exploits the well-known method of unilateralization for speeding up amplifiers [7].

In summary, the use of distributed amplification, adaptive loop gain, and unilateralization help improve the transimpedance amplifier of Fig. 3 to the energy-efficient version of Fig. 4.

B. Probe

In our pulse oximeter, we employ a finger clip transmittance reusable probe manufactured by Nonin Medical, Inc. (model
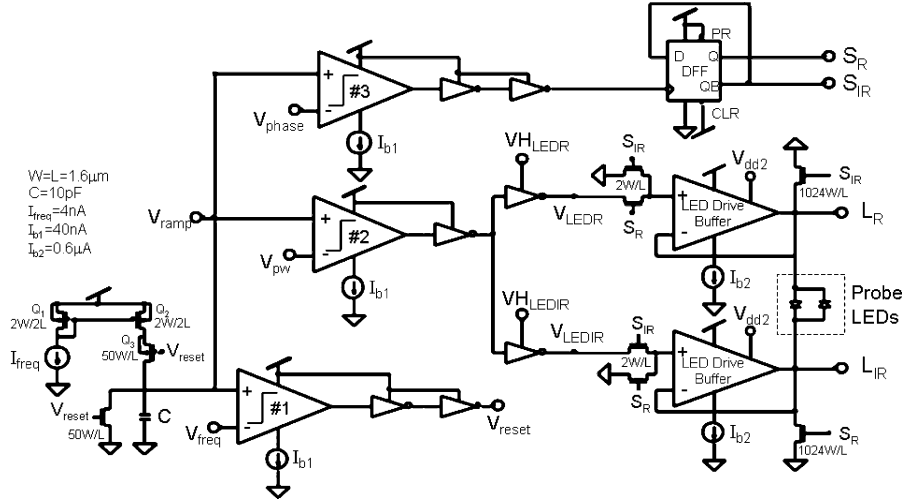
Fig. 6.   Circuit implementation of the "oscillator/LED and switching control" block used in our pulse oximeter system of Fig. 1. (All MOS transistors in this figure are NMOS, except Q1-Q3 which are PMOS.)

8000AA) as the sensing element. As previously mentioned, the probe consists of two small and high-intensity red and IR LEDs and a silicon photodiode placed on the opposite side of the LEDs. They are all housed in an optically shielded package that is coated with black material in its interior (to prevent unwanted reflection and optical interference) and an opaque plastic cover on its exterior. To minimize the number of wires in the probe (and, hence, cost), the LEDs are wired in a parallel arrangement with polarities reversed. To construct our oximeter, besides the LEDs and optical shield, we removed all other components of the Nonin's system and completely replaced them with ours.

C. Oscillator/LED and Switching Control

This block, whose circuit implementation is shown in Fig. 6, is responsible for generating and synchronizing the required LED drive and current switching pulses in Fig. 1. The core of this block is a relaxation oscillator which takes advantage of the periodic charging/discharging of a capacitor to generate an oscillation at an adjustable switching frequency f_s. This core, seen in the bottom left corner of Fig. 6, consists of a current source (I_{freq}), a capacitor (C), a comparator (#1), and switches to reset the voltage of the capacitor. The generated oscillating ramp signal is used by other comparators, DFF, and switches to produce and synchronize the LED drive (L_R/L_{IR}) and current switching (S_R/S_{IR}) pulses.

This block also supplies the milliampere current levels required to illuminate LEDs by the employment of two "LED drive buffers" which are essentially voltage buffers designed to provide a large amount of currents to their output load. The circuit structure of each buffer is composed of a conventional differential pair amplifier followed by a Class AB output stage [12].

Note that our "oscillator/LED and switching control" is designed to be fully programmable. Specifically, the user can adjust the pulse frequency, the LED pulse amplitude, the LED pulsewidth (or duty cycle), and the relative phase between the LED and switching pulses by controlling I_{freq}, VH_{LEDR}/VH_{LEDIR}, V_{pw}, and V_{phase}, respectively.
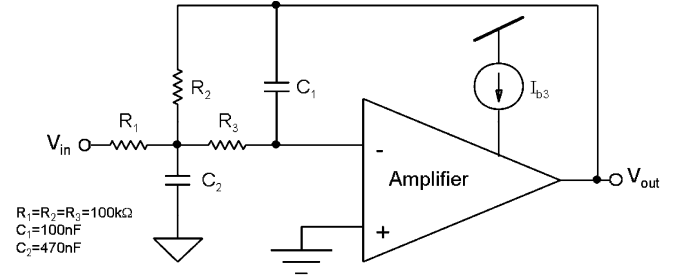

Fig. 7.   Topology of a standard active second-order low-pass filter (each low-pass filter in Fig. 1 is formed by cascading two instances of this second-order filter).

D. Low-Pass Filters (LPFs)

LPFs are placed after transimpedance amplifiers in our pulse oximeter system of Fig. 1 to attenuate switching frequency components and extract blood pulsation signals. Each filter in Fig. 1 has a fourth-order rolloff achieved by cascading two standard active second-order Butterworth LPFs with the topology displayed in Fig. 7. It is straightforward to find the transfer function of this circuit to be

$$H(s) = \frac{V_{out}}{V_{in}}$$
$$= \frac{-1}{s^2 R_1 R_3 C_1 C_2 + s C_1 \left(R_1 + R_3 + \frac{R_1 R_3}{R_2} \right) + \frac{R_1}{R_2}}$$
$$= \frac{A_v}{\tau^2 s^2 + \frac{\tau}{Q} s + 1}. \tag{5}$$

Commercial pulse oximeters are generally designed to handle a wide range of pulse rates (i.e., between 18–300 bpm or, equivalently, 0.3–5 Hz in frequency). We designed our system for this operating range as well. These specifications imply that the corner frequency of our LPFs needs to be low enough to remove switching components (at $f_s = 100$ Hz in our setup) as far as possible, but not very low to prevent the attenuation of the signals in the passband of interest (which extends up to 5 Hz). Hence, we design the LPF corner frequency to be around
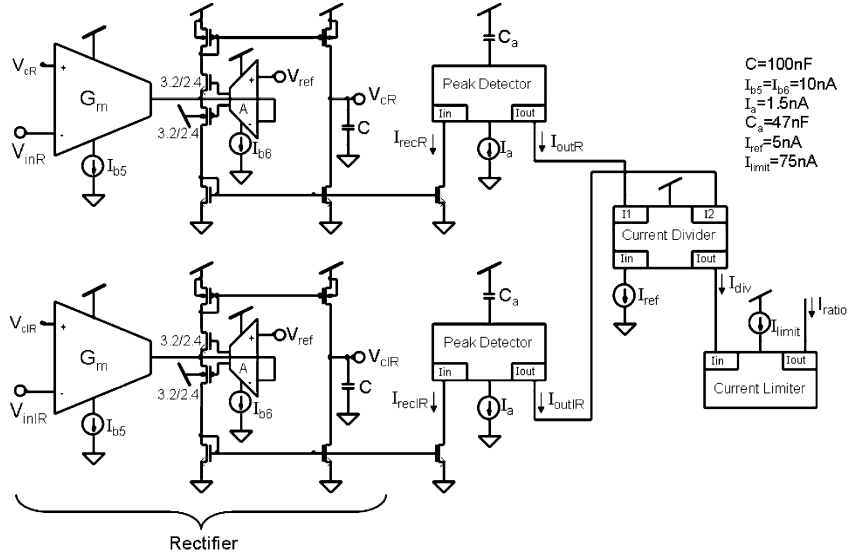
Fig. 8. Structure of the "ratio computation" block employed in our pulse oximeter system of Fig. 1. (Unless otherwise specified, all of the transistors in this figure have $W = 32\ \mu$m and $L = 3.2\ \mu$m.)

7 Hz and choose values for resistors and capacitors in Fig. 7 accordingly (the resistors are on-chip; however, the capacitors are off-chip). As the active element of our filter, we utilize a classic two-stage operational amplifier (a differential amplifier followed by a common-source stage) [12], [13] with a Class AB output stage. The LPFs described here are not power efficient and were merely chosen for their simplicity, since their power consumption has little impact on the power of the overall pulse oximeter, which is dominated by that of the LED and transimpedance amplifier. Other transconductance-capacitor filters as described in [18] can lower the power of these filters further. The designed filters must be at least fourth order to help attenuate aliasing artifacts caused by sampling and duty cycling.

E. Ratio Computation

Fig. 8 illustrates the structure of our "ratio computation" block employed at the last stage of our pulse oximeter to compute R. This block first detects the amplitudes of the red and IR blood pulsation signals (extracted by LPFs) through two modified current-mode envelope detectors and then computes their ratio by the use of a translinear current divider to find R [see (2)].

The circuit implementation of the envelope detectors is based on the designs presented in [14] and [15]. Each envelope detector is composed of a half-wave voltage-to-current-converting rectifier followed by a peak detector. The V-I conversion is performed through a transconductance amplifier (G_m in Fig. 8). The current through the capacitor C is split into a positive half and a negative half by an intervening a Class B mirror and only the negative half is mirrored to the input of the peak detector. The capacitor's current is a high-pass-filtered version of the input voltage with its pole at $G_m/2\pi C$ (set to be 0.1 Hz in our design). Thus, the response of the rectifier is not sensitive to input dc voltage, and the offsets of the preceding blocks do not matter. The rectifier also features active feedback and dead-zone reduction schemes achieved by the use of a feedback amplifier A in Fig. 8, [14].
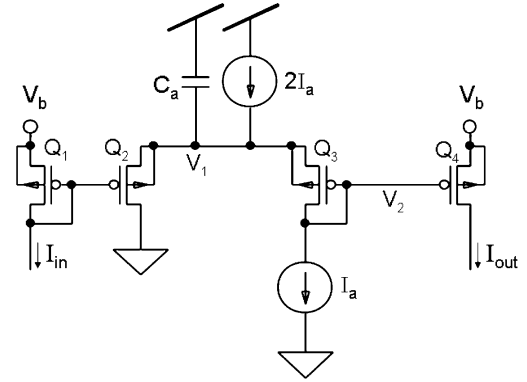

Fig. 9. Circuit schematic for each peak detector utilized in the "ratio computation" block of Fig. 8. (All of the transistors in this figure have $W = 64\ \mu$m and $L = 3.2\ \mu$m.)

The circuit schematic for each peak detector used in Fig. 8 is shown in Fig. 9. This circuit is essentially a current-mode first-order LPF topology [16] that estimates the average of the rectified signal as being representative of its energy and exploits the translinear principle in its design. It can be shown [17] that the pole frequency of the circuit in Fig. 9 is at $\kappa_p I_a/2\pi C_a U_T$ (designed to be 0.15 Hz in our pulse oximetry application).

Fig. 10(a) shows the circuit schematic of the current divider circuit employed in the structure of Fig. 8. By applying the current-mode translinear principle [17], we can easily find the input–output relationship of this circuit to be $I_{out} = I_{ref}(I_1/I_2)$.

A problem that always arises in division or ratio circuits is that of dividing by zero when there is no input: When no tissue is present inside the oximeter's probe and, thus, no blood pulsation signals are detected, the output currents of the peak detectors in Fig. 8 (I_{outR} and I_{outIR}) are nearly zero. Consequently, a $0/0$ division in the current divider causes its output to become very large. This scenario significantly hurts the power consumption of the pulse oximeter system when it is in standby mode. Our
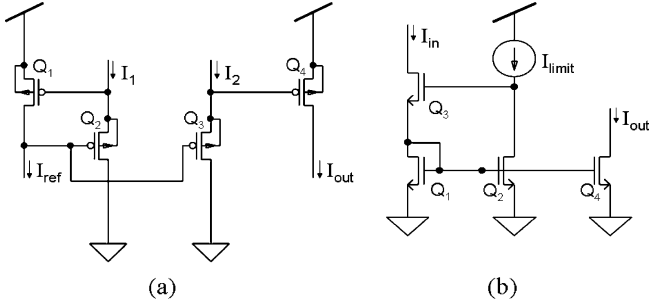
Fig. 10. Circuit schematic of (a) the current divider and (b) the current limiter employed in the "ratio computation" block of Fig. 8. (All of the transistors in Fig. 10(a) have W $= 64\,\mu$m and L $= 3.2\,\mu$m. All of the transistors in Fig. 10(b) have W $= 32\,\mu$m and L $= 3.2\,\mu$m.)

Fig. 11. Die photograph of our pulse oximeter chip with its building blocks marked (fabricated in a 1.5-μm AMI BiCMOS process).

solution is to employ a current-limiter block as the last section of the ratio computation as shown in Fig. 8. This current limiter imposes a ceiling on the magnitude of the output current. The circuit implementation of our current limiter is illustrated in Fig. 10(b) and is based on a design previously used in [18]. This circuit adapts a standard Wilson current mirror configuration [12] to have two inputs; negative feedback automatically drives the transistors that supply $I_{\mathrm{in}}(= I_{\mathrm{div}})$ or I_{limit} out of saturation and reduces their currents to that of the smaller input. The current output of the circuit is always the smaller of its two inputs. Thus, the current-limiting circuit ensures that the output of the pulse oximeter, which represents R, is limited to a maximum value of I_{limit}.

Finally, we conclude that when our pulse oximeter is measuring the blood's oxygen saturation of a subject under test I_{ratio} (which constitutes the output of our whole pulse oximeter system shown in Fig. 1) is equal to

$$I_{\mathrm{ratio}} = I_{\mathrm{div}} = I_{\mathrm{ref}} \times \frac{I_{\mathrm{outR}}}{I_{\mathrm{outIR}}} = I_{\mathrm{ref}} \times \frac{v_{\mathrm{in}R}^{(4)}}{v_{\mathrm{inIR}}}$$
$$= I_{\mathrm{ref}} \times \frac{i_{\mathrm{ac},R}/I_{\mathrm{DC},R}^{(2)}}{i_{\mathrm{ac,IR}}/I_{\mathrm{DC,IR}}} = I_{\mathrm{ref}} \times R. \qquad (6)$$

Thus, as mentioned before, the output of our pulse oximeter chip is directly proportional to R. If a digital output is desired, then we can obtain a digital representation of R by computing $I_{\mathrm{ratio}}/I_{\mathrm{ref}}$ with an 8-b version of an energy-efficient current-mode analog-to-digital converter (ADC) consuming a few microwatts of power, such as the one described in [19]. Computational ADCs discussed in [24] can provide automatic calibration of the final current output as well as compute polynomial functions of R (see (7) that is described later) that encode the oxygen saturation.

F. Reference Generator/Bias Circuitry

To attain temperature immunity and minimize the effects of power-supply noise, all the necessary bias currents and voltages needed by different circuits throughout our pulse oximeter system are created on-chip by a reference and then properly distributed to our low-power circuits through current mirroring and buffering. The core of this block is a thermal-voltage-referenced self-biased current source with appropriate startup circuitry described in [15]. The topology of this reference generator is ex-
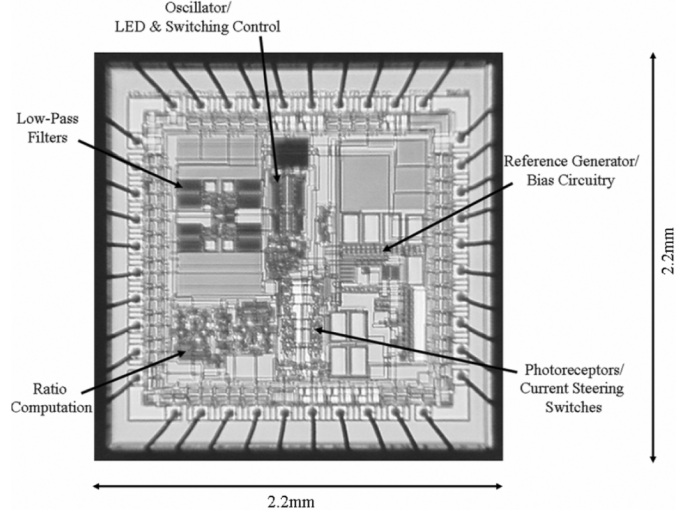
tensively discussed in [22] along with a history of its evolution. Although this reference has very good immunity to power-supply noise, we utilized cascode mirroring and capacitive bypassing to further reduce the small remaining power-supply effects on our reference output.

IV. EXPERIMENTAL RESULTS

Fig. 11 shows a die photograph of the chip containing the entire low-power pulse oximeter system shown in Fig. 1. The chip was fabricated in a 1.5-μm AMI BiCMOS n-well process available through MOSIS. All of the pulse oximeter building blocks are also marked in this figure. These blocks were individually fabricated on previous chips, tested, and debugged before all being fit into the complete pulse oximeter chip of Fig. 11, which is 2.2 mm × 2.2 mm in size. The experimental tests are all run on a 5-V power supply.

The experimental output voltage waveforms that typically appear at the output of the logarithmic transimpedance amplifiers (i.e., Vout$_R$ and Vout$_{IR}$ in Fig. 1) are shown in Fig. 12. These waveforms are measured in the case when a finger has been placed in the oximeter probe. The LED pulses (L$_R$ and L$_{IR}$), running at a frequency f_s of 100 Hz each with a duty cycle of approximately 3%, are displayed in this figure as well. We observe that Vout$_R$ and Vout$_{IR}$ are composed of pulses that are responsive to the light pulses generated by red and IR LEDs, respectively. This verifies that each transimpedance amplifier responds only to its designated input light signal and, hence, the photocurrent splitting is successfully performed by the current steering block.

What the reader cannot observe in Fig. 12 is that the amplitudes of the fast pulses of Vout$_R$ and Vout$_{IR}$ are slowly vibrating with a frequency equal to the heart rate of the subject under test (fp). In other words, blood pulsations have AM modulated the voltage pulses at the output of the transimpedance amplifiers as predicted. These blood pulsation signals are extracted by the LPFs that follow the amplifiers and appear at the output of these filters as displayed in Fig. 13. These are the red and IR blood pulsation signals of a subject measured by our
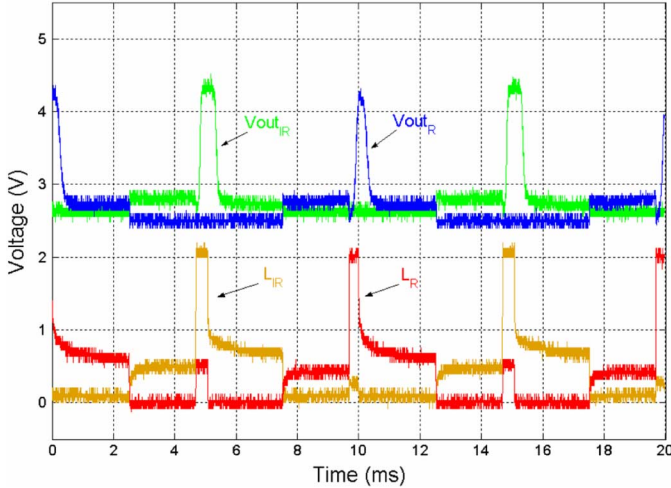
Fig. 12. Voltage waveforms measured at the output of the two logarithmic transimpedance amplifiers shown in our pulse oximeter system of Fig. 1.

Fig. 14. Second-order empirical calibration curve relating the output current of our pulse oximeter to the blood oxygen saturation of the subject under test.
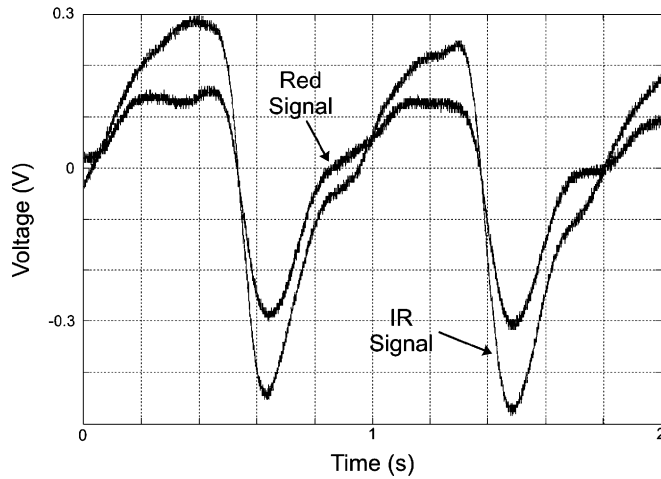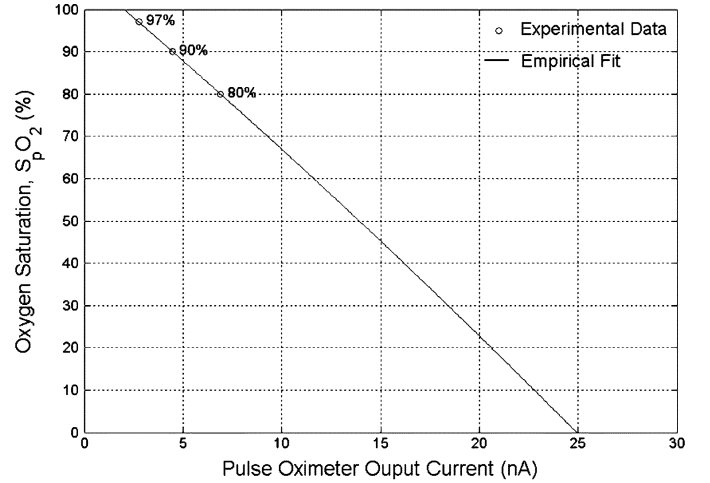

Fig. 13. Measured blood pulsation signals of a subject under test. These waveforms appear at the outputs of the two LPFs shown in our pulse oximeter system of Fig. 1.

pulse oximeter. They are also called plethysmographic (or photoplethysmographic) signals in pulse oximetry. Although the absolute amplitudes of these signals are rather low, our system is sensitive enough to detect them (because our system is only limited by the shot noise of the incoming light). The waveforms shown in Fig. 13 represent internal waveforms from the pulse-oximeter chip. These waveforms were amplified by a $\sim 100 \times$ external off-chip amplifier with limited bandwidth to ensure that we could clearly view them on an oscilloscope without being limited by oscilloscope noise. Future versions of the chip can incorporate on-chip micropower versions of such amplifiers [21] that consume less than 1% of total oximeter power. As we discuss later, our oximeter power is dominated by the LED.

The plethysmographic signals of Fig. 13 provide valuable information about the physiological conditions of the subject under test. For instance, we can measure the heart rate of the subject from these signals. More important, the ratio of the red over IR signal of the subject determines R which is directly related to her blood oxygen saturation (S_pO_2).

In Section II, we mentioned that all pulse oximeters and our own require calibration to relate R to S_pO_2. To perform such calibration, we used commercially available devices that simulate the optical properties of the human finger. Specifically, we utilized three BC Biomedical FingerSim translucent artificial fingers that are built with colored materials to simulate arterial blood at 80%, 90%, and 97% oxygen saturation levels, respectively.

To calibrate our pulse oximeter, we placed each of these calibration fingers inside its probe, manually pressed the fingers as instructed, and measured the output current of our oximeter. With these three available data points (each of which is an average value of 180 current readings), we can plot an exact second-oder polynomial curve which is the relationship utilized in most commercial pulse oximeters as well [1]. This calibration curve is plotted in Fig. 14 and is important because it relates the output current of our oximeter chip I_{ratio} (adjusted to be $I_{ref} \times R = 5\,nA \times R$ in our setup) to the oxygen saturation of the subject under test. Mathematically, this relationship can be expressed as

$$S_pO_2 = 108 - 4.0 \times 10^9 I_{ratio} - 1.5 \times 10^{16} I_{ratio}^2$$
$$= 108 - 20R - 0.375R^2. \quad (7)$$

After we calibrated the pulse oximeter, we measured the blood oxygen saturation of real subjects with our sensor and compared the readings with a reference. We utilized a commercial Nonin digital handheld pulse oximeter, model PalmSAT 2500, as our [20] Table I lists the oxygen saturation (S_pO_2) of various individuals measured by our and this reference pulse oximeter at the same time. The output current readings of our pulse oximeter associated with each subject are also reported in this table. By statistically analyzing the differences between the oxygen readings of our pulse oximeter and the reference oximeter, we find that our oximeter differs from the Nonin readings by a mean of -1.2% and the standard deviation of differences is 1.5%. Since the accuracy of most oximeters is approximately 2% [1] and the medical use of pulse oximetry

TABLE I
BLOOD OXYGEN SATURATION OF VARIOUS SUBJECTS MEASURED BY OUR
AND A REFERENCE PULSE OXIMETER

Subject	Our Pulse Oximeter Output Current (I_{ratio}) Readings	Our Pulse Oximeter Oxygen Saturation (S_pO_2) Readings	Reference Pulse Oximeter Oxygen Saturation (S_pO_2) Readings
# 1	3.2nA	95%	98%
# 2	3.1nA	95%	97%
# 3	3.6nA	93%	95%
# 4	3.3nA	95%	95%
# 5	2.9nA	96%	95%
# 6	3.2nA	95%	97%
# 7	3.0nA	96%	95%
# 8	2.9nA	96%	98%
# 9	2.8nA	96%	99%
# 10	3.1nA	95%	95%
# 11	2.8nA	97%	98%

TABLE II
MEASURED POWER DISSIPATION FOR EACH INDIVIDUAL BLOCK OF OUR PULSE
OXIMETER SYSTEM SHOWN IN FIG. 1

Power Consumption per Block	Value
Oscillator/LED & Switching Control	4.4mW
Two Transimpedance Amplifiers	80μW
Two Low-pass Filters	300μW
Ratio Computation	2.2μW
Reference Generator/Bias Circuitry	11.5μW
Total	4.8mW

Less than 400μW of processing power

TABLE III
COMPARISON OF THE POWER CONSUMPTION OF OUR PULSE OXIMETER WITH A
NUMBER OF STATE-OF-THE-ART LOW-POWER COMMERCIAL PULSE OXIMETERS

Pulse Oximeter Version	Total Power Consumption (LED power and processing power, excluding display)	Days in Operation on 4 "AAA" Batteries
Our Chip	4.8mW	60
WristOx® 3100	~55mW	5.2
Xpod	60mW	4.8
Ipod	60mW	4.8
Avant® 4000	71mW	4
PalmSAT® 2500	~80mW	3.6
Onyx® 9500	~120mW	2.4
8500 Series	~130mW	2.2

does not require precision beyond this level, our oximeter represents a commercially viable solution.

Our primary objective in designing a new pulse oximeter was to reduce its power consumption as far as possible without sacrificing any of its critical medical properties. Therefore, we carefully examined the power requirement of various stages of our pulse oximeter. The measured power dissipation of each building blocks of our system is listed in Table II. We observe that the total power consumption of our pulse oximeter adds up to 4.8 mW. We notice that the power dissipation of the "oscillator/LED & switching control" block, which is mostly spent to drive and illuminate the two red and IR LEDs, dominates the power requirement of the whole pulse oximeter system. In fact, the total power dissipation of all the other parts of the system, which constitute the oximeter's processing unit, does not exceed 400 μW or 8.5% of the total power.

Finally, Table III compares the total power dissipation of our pulse oximeter with several low-power commercial pulse oximeters manufactured by Nonin, Inc., a company whose products are currently the state of the art in low-power portable oximeters. Using a multimeter, we directly measured the current that is drawn from the batteries of these oximeters with the display inactive and active. The numbers reported in Table III do not include display power consumption, just LED and processing power. We observe that our oximeter consumes about 11 times less power than the lowest-power commercial pulse oximeter that we could find and measure (model WristOx 3100). The tangible consequence of these power savings is

that while the batteries in the WristOx 3100 oximeter need replacement/recharging every five days, the same batteries can power up our pulse oximeter for two months.

Although our fabricated pulse oximeter currently dissipates considerably less power than other existing oximeters, it is possible to reduce the power consumption of our oximeter even further to around 1 mW with more area consumption as described in the Appendix. The use of a submicron technology (we used 1.5 μm) could yield improvements as well. Beyond this optimal point, our transimpedance amplifiers would have to burn more power than our LEDs to sense their reduced input light intensity so that the total power requirement of the oximeter would rise again.

V. SUMMARY

Our low-power pulse oximeter achieved more than an order-of-magnitude reduction in power consumption over the best commercial pulse oximeters, and yielded similar performance as we confirmed with experimental measurements. Most of this reduction was due to the use of a novel energy-efficient transimpedance amplifier that was inherently sensitive to the signals required for pulse oximetry computations, and which was built with distributed amplification, adaptive loop gain control, and unilateralization. Consequently, the dominant source of power consumption, LED power, could be significantly reduced. Our oximeter is suited for use in emerging portable and wearable medical applications where battery life is of paramount concern.

Simple extensions to our adaptive energy-efficient transimpedance amplifier that we outline in the following Appendix suggest that submilliwatt oximetry without compromising performance could be possible in the future. Several simple extensions to our circuits are also possible in future designs to increase programmability, subtract out ambient light, to implement multiwavelength oximetry, to work with digitized outputs of the transimpedance amplifier to remove motion artifacts via digital signal processing, to adapt the LED power to the subject, etc. Thus, this paper should be seen as representative of the powerful benefits of our transimpedance amplifier in low-power pulse oximetry rather than as a final design.

APPENDIX
Lower Bound on Power Consumption, Noise, and Minimum Detectable Contrast of Pulse Oximeter

Although we cannot increase the gain of the amplifier used in our transimpedance amplifier circuit beyond its current (very large) value due to voltage-headroom limitations, the reader might wonder how much further we could reduce the total power consumption of our pulse oximeter if we did not face this gain constraint.

It can be shown that the closed-loop bandwidth (BW) of the transimpedance amplifier shown in Fig. 4 in terms of the photocurrent (I_l) and amplifier's gain (A_{amp}) is calculated by

$$
\begin{aligned}
\text{BW} &= \frac{1}{2\pi T_{\text{in}}} \times (1 + A_{lp}) \\
&\approx \frac{I_l}{2\pi U_T C_{\text{in}}} \times A_{\text{amp}} \times \left(\frac{\kappa_1 C_1}{C_1 + C_2} \right).
\end{aligned} \quad (8)
$$

The BW has to always be larger than a certain limit so that the photoreceptors completely turn ON and settle down in the short ON duration of LED pulses to ensure proper conversion, distribution, and processing of the input red and IR photocurrents (e.g., $\text{BW} = 2.1$ kHz in our design). Also, note that I_l is directly proportional to the drive current of LEDs or, equivalently, to the LED power (P_{LED}). Thus, for a fixed BW, we can write[1]

$$
\begin{aligned}
\frac{I_l'}{I_l} &= \frac{P_{\text{LED}}'}{P_{\text{LED}}} = \frac{A_{\text{amp}}}{A_{\text{amp}}'} \Rightarrow P_{\text{LED}}' \\
&= 4.4 \text{ mW} \times \frac{A_{\text{amp}}}{A_{\text{amp}}'} = (4.4 \text{ mW})x^{-1}
\end{aligned} \quad (9)
$$

where $P_{\text{LED}} = 4.4$ mW is the LED power at its current setting (see Table II) and $x = A_{\text{amp}}'/A_{\text{amp}}$ is equal to the extra gain that the amplifier needs at the optimum condition (this will be calculated).

We need to express the power consumption of photoreceptors (P_{PR}) in terms of x as well. We assume that the majority of this power is burnt within transconductors OTA1 in the circuit of Fig. 4 to provide a large gain for the distributed amplifier and speed up the input light pole. Consequently, we have

$$
\begin{aligned}
\frac{P_{\text{PR}}'}{P_{\text{PR}}} &\simeq \frac{I_l'}{I_l} = \left(\frac{G_{m1}'}{G_{m1}} \right)^2 = \left(\frac{A_{\text{amp}}'}{A_{\text{amp}}} \right)^{2/3} \Rightarrow P_{\text{PR}}' \\
&= 80 \ \mu\text{W} \times \left(\frac{A_{\text{amp}}'}{(A_{\text{amp}})} \right)^{2/3} = (80 \ \mu\text{W})x^{2/3}
\end{aligned} \quad (10)
$$

where $P_{\text{PR}} = 80 \ \mu\text{W}$ is the current value for photoreceptors power (see Table II) and we assume that the transistors in OTA1 are operating above threshold because their bias current (I_1) is relatively large.

Ignoring the power dissipations of the two LPFs: 1) , the "ratio computation" block and 2) the "reference generator/bias

---

circuitry" block, we can approximate that the overall power requirement of our pulse oximeter is determined by the LEDs and photoreceptors. Therefore

$$
\begin{aligned}
P_{\text{TOT}}'(x) \simeq P_{\text{LED}}' + P_{\text{PR}}' &= (4.4 \text{ mW})x^{-1} \\
&+ (80 \ \mu\text{W})x^{2/3}. \quad (11)
\end{aligned}
$$

From this equation, we expect that there should be an optimum point in which the total power consumption of our oximeter (P_{TOT}) has a minimum. The analysis shows that this optimum occurs at $x = 14.1$, indicating that if we could increase the amplifier's gain by a factor of 14.1, we would reduce the total power dissipation to $P_{\text{TOT}}' = 780 \ \mu\text{W}$, a factor of 5.7 lower than its current value of $P_{\text{TOT}} = 4.48$ mW. Note that making the gain larger than this optimum would not help because the photoreceptor power would exceed the LED power and hurt the total power dissipation of the sensor.

The 14.1 decrease in LED power could be accomplished by either reducing the LED drive currents by this factor or lowering the duty cycle of the chopped LED pulses. In any case, the average LED-generated photocurrent would drop from its current 50-nA value (typically) to about 3.5 nA.

We also need to make sure that two other factors, namely: 1) ambient light and 2) minimum detectable contrast of the sensor do not limit the performance of our pulse oximeter at such reduced LED power. The photocurrent produced in the photodiode due to ambient light in our existing setup is about 3 nA, still smaller than our LED-generated photocurrent. Well-known techniques to subtract the ambient light in a calibration phase may be used although we have not done so in this implementation at our current light levels since we did not need to. Also, we need to calculate the minimum detectable contrast of our transimpedance amplifier at this photocurrent level to make sure that it is still lower than 0.5%, the smallest contrast (ac/dc) of the blood-modulated input light we typically encounter in pulse oximetry [1]. We now show that it is less than 0.1% even at such low light levels.

The total voltage noise contributed by all of the blocks in Fig. 1 referred to the output of the logarithmic transimpedance amplifiers and shows that the oximeter's noise is dominated by the noise of its front-end transimpedance amplifiers as it should be in any good design. Dividing this noise by the gain relationship of (4), we find the minimum detectable contrast to be

$$
\left(\frac{i_{\text{ac},l}}{I_{\text{DC},l}} \right)_{\text{min}} = \sqrt{\frac{2\pi q \times \text{BW}}{I_{\text{DC},l}}} \quad (12)
$$

where $I_{\text{DC,l}}$ is the average photocurrent flowing into the transimpedance amplifiers. Even with $I_{\text{DC,l}} = 3.5$ nA, the minimum detectable contrast is less than 0.1%.

The extra 14.1 increase in the gain of the distributed amplifier in Fig. 4 could be achieved by supplying 5.8 times more bias current I_l to OTA1 transconductors. This strategy would cause a 2.4-fold rise in the voltage overdrive of the transistors in OTA1 or require the use of 5.8 times wider transistors to keep their voltage overdrive at the current level.

---

[1]In this Appendix, "parameter$^/$" and "parameter" represent the optimum and current values of a parameter which are used in our analysis, respectively.

ACKNOWLEDGMENT

REFERENCES

[1] J. G. Webster, *Design of Pulse Oximeters*. Bristol, U.K.: Inst. Phys.., 1997.

[2] C. A. Mead, *Analog VLSI and Neural Systems*. Reading, MA: Addison-Wesley, 1989.

[3] T. Delbruck and C. Mead, "Adaptive photoreceptor with wide dynamic range," in *Proc. IEEE Int. Symp. Circuits and Systems*, May 1994, vol. 4, pp. 339–342.

[4] T. Delbruck and C. A. Mead, "Analog VLSI phototransduction by continuous-time, adaptive, logarithmic photoreceptor circuits," *Caltech Computation Neural Syst. Memo.*, no. 30, Feb. 1995.

[5] D. A. Baylor, G. Matthews, and K.-W. Yau, "Two components of electrical dark noise in toad rod outer segments," *J. Physiol.*, vol. 309, pp. 591–621, 1980.

[6] L. Stryer, "Cyclic GMP cascade of vision," *Annu. Rev. Neurosci.*, vol. 9, pp. 87–119, 1986.

[7] T. H. Lee, *The Design of CMOS Radio-Frequency Integrated Circuits*. Cambridge, U.K.: Cambridge Univ. Press, 1998.

[8] R. Sarpeshkar, R. F. Lyon, and C. A. Mead, "A low-power wide-dynamic-range analog VLSI cochlea," *Analog Integr. Circuits Signal Process.*, vol. 16, pp. 245–274, 1998.

[9] R. Sarpeshkar, "Traveling waves versus bandpass filters: The silicon and biological cochlea," in *Proc. Int. Symp. Recent Developments in Auditory Mechanics*, H. Wada, Ed. *et al.*, 2000, pp. 216–222, World Scientific.

[10] R. Sarpeshkar, R. F. Lyon, and C. A. Mead, "A low-power wide-linear-range transconductance amplifier," *Analog Integr. Circuits Signal Process.*, vol. 13, no. 1/2, pp. 123–151, May/Jun. 1997.

[11] M. Tavakoli and R. Sarpeshkar, "A sinh resistor and its application to tanh linearization," *IEEE J. Solid-State Circuits*, vol. 40, no. 2, pp. 536–543, Feb. 2005.

[12] P. R. Gray, P. J. Hurst, S. H. Lewis, and R. G. Meyer, *Analysis and Design of Analog Integrated Circuits*, 4th ed. New York: Wiley, 2001.

[13] D. A. Johns and K. Martin, *Analog Integrated Circuit Design*. New York: Wiley, 1997.

[14] S. M. Zhak, M. W. Baker, and R. Sarpeshkar, "A low-power wide dynamic range envelope detector," *IEEE J. Solid-State Circuits*, vol. 38, no. 10, pp. 1750–1753, Oct. 2003.

[15] R. Sarpeshkar, C. Salthouse, J.-J. Sit, M. W. Baker, S. M. Zhak, T. K.-T. Lu, L. Turicchia, and S. Balster, "An ultra-low-power programmable analog bionic ear processor," *IEEE Tran. Biomed. Eng.*, vol. 52, no. 4, pp. 711–727, Apr. 2005.

[16] D. R. Frey, "Log-domain filtering: An approach to current-mode filtering," *Proc. Inst. Electr. Eng.*, vol. 140, pt. G, pp. 406–416, 1993.

[17] S.-C. Liu, J. Kramer, G. Indiveri, T. Delbruck, and R. Douglas, *Analog VLSI: Circuits and Principles*. Cambridge, MA: MIT Press, 2002.

[18] R. Sarpeshkar, M. W. Baker, C. D. Salthouse, J.-J. Sit, L. Turicchia, and S. M. Zhak, "An analog bionic ear processor with zero-crossing detection," in *Proc. IEEE Int. Solid-State Circuits Conf. Dig. Tech. Papers*, San Francisco, CA, Feb. 2005, vol. 48, pp. 78–79.

[19] H. Y. Yang and R. Sarpeshkar, "A time-based energy-efficient analog-to-digital converter," *IEEE J. Solid-State Circuits*, vol. 40, no. 8, pp. 1590–1601, Aug. 2005.

[20] *PalmSAT® 2500 Digital Handheld Pulse Oximeter User Guide*. Minneapolis, MN: Nonin Medical, 2004.

[21] W. Wattanapanitch and R. Sarpeshkar, "An energy-efficient micropower neural recording amplifier," *IEEE Trans. Biomed. Circuits Syst.*, vol. 1, no. 2, pp. 136–147, Jun. 2007.

[22] T. Delbrück and A. van Schaik, "Bias current generators with wide dynamic range," *Analog Integr. Circuits Signal Process.*, vol. 43, no. 2, pp. 247–268, 2005.

[23] A. Basu, R. W. Robucci, and P. E. Hasler, "A low-power, compact, adaptive logarithmic transimpedance amplifier operating over seven decades of current," *IEEE Trans. Circuits Syst. I, Reg. Papers*, vol. 54, no. 10, pp. 2167–77, Oct. 2007.

[24] H. Yang and R. Sarpeshkar, "A bio-inspired ultra-energy-efficient analog-to-digital converter for biomedical applications," *IEEE Trans. Circuits Syst. I*, vol. 53, no. 11, pp. 2349–2356, Nov. 2006, special issue on Life Sciences and System Applications.

Maziar Tavakoli (S'98) received the B.Sc. degree in electrical engineering from Sharif University of Technology, Tehran, Iran, in 1998 and the M.Sc. and Ph.D. degrees in electrical engineering from the Massachusetts Institute of Technology (MIT), Cambridge, in 2001 and 2005, respectively.

At MIT, he worked on developing high-performance electronics for microelectromechanical-system vibration sensors and pulse oximeters. His research interests included analog very-large-scale integrated circuit design for biomedical and sensory systems. Currently, he is with Linear Technology Corp., North Chelmsford, MA.

Lorenzo Turicchia received the Laurea degree in electrical engineering from the University of Padova, Padova, Italy, and the Ph.D. degree in computer science from the University of Udine, Udine, Italy.

In 2002, he joined the Analog VLSI and Biological Systems Group in the Department of Electrical Engineering and Computer Science, Massachusetts Institute of Technology (MIT), Cambridge, where he completed his doctoral research and is now a Research Scientist. His main research interests are in nonlinear signal processing, especially for audio and biomedical applications, and bioelectronics. His work has included research on cochlear implants for the hearing impaired, visual prostheses for the blind, speech prostheses for individuals with severe communication disabilities, automatic speech recognition in noise, and wearable medical devices. In these areas, he has authored seven patent applications and many publications. He is currently working on robust techniques for the recognition of speech, speaker, and language in noisy environments; bioelectronics for wearable and implantable medical devices; and neural decoding techniques for neural prosthetic devices for paralysis.

Rahul Sarpeshkar (SM'07) received the Bachelor's degrees in electrical engineering and physics from the Massachusetts Institute of Technology (MIT), Cambridge, and the Ph.D. degree from the California Institute of Technology (Caltech), Pasadena.

After completing the Ph.D. degree at Caltech, he joined Bell Labs as a member of the technical staff. Since 1999, he has been on the faculty of MIT's Electrical Engineering and Computer Science Department where he heads a research group on Analog VLSI and biological Systems, and is currently an Associate Professor. His research interests include analog microelectronics, ultra-low power circuits and systems, biologically inspired circuits and systems, biomedical systems, feedback systems, neuroscience, and molecular biology.

Dr. Sarpeshkar has received several awards, including the Packard Fellow award given to outstanding faculty, the ONR Young Investigator Award, the National Science Foundation Career Award, the Indus Technovator Award, and the junior Bose award for excellence in teaching. He holds more than 25 patents and has authored many publications, including one that was featured on the cover of *Nature*.